Chaotic Modeling and Simulation (CMSIM) 1: 173–186, 2011

Simulations of the Frequency Modulated - Atomic Force Microscope (FM-AFM) Nonlinear Control System

Átila M. Bueno[1], José M. Balthazar[1], and José R. C. Piqueira[2]

[1] Universidade Estadual Paulista UNESP, Departamento de Estatística Matemática Aplicada e Computação DEMAC/IGCE, Rio Claro, SP, CP 178, CEP 13506-900, Brazil
(E-mail: `atila@lac.usp.br`, `jmbaltha@rc.unesp.br`)

[2] Escola Politécnica, Universidade de São Paulo, Av. Prof. Luciano Gualberto, travessa 3, n. 158, 05508-900, São Paulo, SP, Brazil
(E-mail: `piqueira@lac.usp.br`)

Abstract. The Frequency Modulated - Atomic Force Microscope (FM-AFM) is a powerful tool to perform surface investigation with true atomic resolution. The control system of the FM-AFM must keep constant both the frequency and amplitude of oscillation of the microcantilever during the scanning process of the sample. However, tip and sample interaction forces cause modulations in the microcantilever motion. A Phase-Locked Loop (PLL) is used as a demodulator and to generate feedback signal to the FM-AFM control system. The PLL performance is vital to the FM-AFM performace since the image information is in the modulated microcantilever motion. Nevertheless, little attention is drawn to PLL performance in the FM-AFM literature. Here, the FM-AFM control system is simulated, comparing the performance for different PLL designs.
Keywords: Frequency Modulated Atomic Force Microscope, Phase-Locked Loops, Synchronization.

1 Introduction

The Atomic Force Microscopy started with the development of the Atomic Force Microscope (AFM) in 1986 by G. Binnig [1]. Simple contact measurement techniques resulted in many discoveries and developments to the surface investigation science. However, contact AFM cannot generate true atomic resolution images in a stable operation, and the samples are frequently damaged due to the contact with the microcantilever tip during the scanning process. On the other hand, noncontact AFM achieve true atomic resolution without damaging the samples.

The Frequency-Modulated Atomic Force Microscope (FM-AFM) is a noncontact AFM technique. In the FM-AFM the microcantilever is deliberately

Received: 12 June 2011 / Accepted: 30 October 2011

ISSN 2241-0503

vibrated (Fig. 1) and is driven to oscillate at a fixed amplitude and frequency [2,3] by the Automatic Gain Control loop (AGC) and by the Automatic Distance Control (ADC) loop, respectively. In addition, the AGC and ADC control systems generate the dissipation and topographic images (Fig. 2).

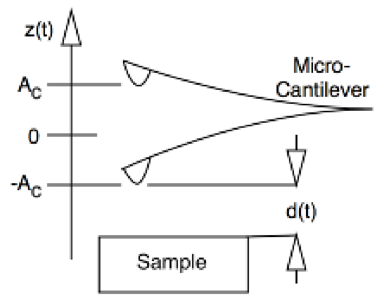

Fig. 1. Schematic view of the microcantilever oscillation

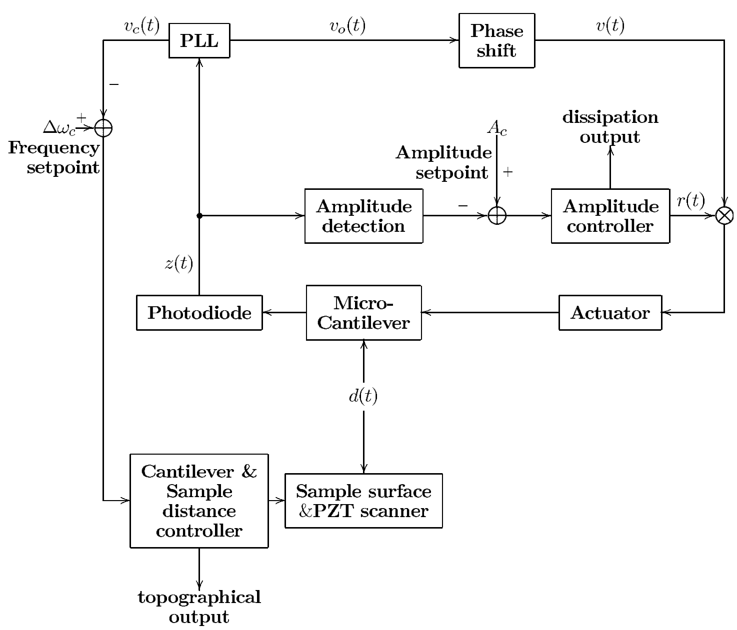

Fig. 2. FM-AFM control system

In the FM-AFM the feedback signal is provided by the Phase-Locked Loop (PLL) present in the FM-AFM control system [4–6] demodulating the tip and sample interaction forces used by the ADC. The PLL also sinthesizes the AGC signal (Fig. 2) in order to control the microcantilever oscillation amplitude.

The PLL (Fig. 3) is control system that synchronizes a local oscillator to an incoming signal, playing important roles in communication, computation and control systems [7,8]. PLLs are nonlinear devices and behaviors such as bifurcations and chaos may arise [9,11]. Additionally, ripple oscillations such as the Double Frequency Jitter (DFJ), generated by the Phase Detector (PD), corrupts the synchronization quality [12]. Therefore, PLL design is crucial to demodulation systems and consequently to FM-AFM.

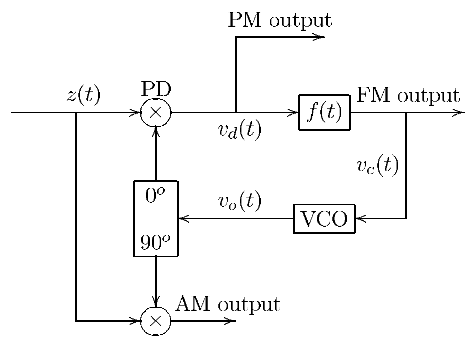

Fig. 3. PLL block diagram

In section 2 the FM-AFM mathematical model is presented. In section 3 the lock-in range of the third order PLL with second order Salley-Key filter is determined by means of bifurcation analysis. In addition a design technique is discussed. In section 4 the simulations results are shown.

2 FM-AFM Mathematical Model

The mathematical model for the FM-AFM is obtained, considering the external driving signal and the tip-sample interaction, the amplitude detector and the PLL. The modeling follows what was presented in [4].

2.1 The Micro-Cantilever

The micro-cantilever is considered to be a damped second order system that can be described by the equation:

$$\ddot{z}(t) + \gamma\dot{z}(t) + \omega_c^2 z(t) = r(t)v(t) + F_{ts}(z, d) \tag{1}$$

where $z(t)$ is the micro-cantilever tip position, γ is the damping factor, ω_c is the natural frequency of the micro-cantilever and d is the tip height (see Fig. 1). $F_{ts}(z, d)$ is the tip and sample interaction force, $r(t)$ controls the amplitude of the oscillation and $v(t)$ is the PLL output signal [2,3,5,6].

The FM-AFM operates in a long range distance between tip and sample, and considering that the tip and sample are not conductive, F_{ts} is mainly due to the van der Waals force, given by:

The photodiode response is considered to be fast, and therefore it is neglected.

$$F_{ts} = \frac{A_H}{6(d(t)+z(t))^2}, \tag{2}$$

where A_H is the Hamaker constant that depends on the type of materials of the tip and sample [3]. It can be seen in Fig. 2 that $r(t)$ is the control signal from the AGC. However, the tip and sample interaction force $F_{ts}(z,d)$ generates modulations on both the amplitude and frequency of the microcantilever motion. For that reason, the micro-cantilever supposedly oscillates according to:

$$z(t) = A(t)\sin(\omega_c t + \varphi_c(t)), \tag{3}$$

where $A(t)$ and $\varphi_c(t)$ carry the modulations generated by the tip and sample interaction. Equation 3 is also the input signal to the PLL, as it can be seen in Fig. 2.

2.2 The Amplitude Detector

The amplitude $A(t)$ of the micro-cantilever and tip oscillation is obtained by a circuit composed of a diode followed by a first-order low pass filter as shown in Fig. 4,

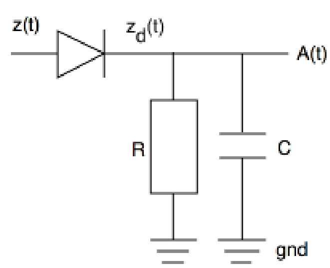

Fig. 4. The amplitude detector.

and the mathematical model of the amplitude detector is given by:

$$\dot{A}(t) + \tau_d A(t) = \tau_d z_d(t), \tag{4}$$

where $\tau_d = \frac{1}{RC}$, and

$$z_d(t) = \begin{cases} z(t), & z(t) > 0 \\ 0, & z(t) \leq 0. \end{cases} \tag{5}$$

2.3 The PLL mathematical model

The PLL is a closed loop control system composed of a phase detector (PD), a low-pass filter $f(t)$ and a voltage controlled oscillator (VCO), that synchronizes the local VCO output to the input signal $z(t)$ (Fig. 3). This is performed by

In the FM-AFM the tip and sample interactions generate frequecy shifts [2].

adjusting the VCO frequency according to $v_c(t)$, which in turn is the filter response to the PD output $v_d(s)$. The output signal is given by:

$$v_o(t) = \mathrm{v}_o \cos\left(\omega_c t + \varphi_o(t)\right), \tag{6}$$

where φ_o is the estimative of the loop to the input phase φ_c (see eq. 3), v_o is the amplitude of the output signal. Since both input and output signals are supposed to have the same central frequency $\omega_c(rad/s)$, the phase error is defined as follows:

$$\vartheta(t) = \varphi_c(t) - \varphi_o(t). \tag{7}$$

Since the AGC keeps the microcantiler amplitude constant, the only parameter that can react to tip and sample forces is the change of the resonant frequency. This shift of frequency is detected and used to change the distance d (Fig. 1), in order to generate topographic images [3]. Consequently, for design and analysis purposes, the input φ_c to the PLL can be written as:

$$\varphi_c(t) = \Omega t. \tag{8}$$

The PLL is described by a differential equation of order $P+1$ [9], considering that the order the filter $f(t)$ is P. The filter transfer function is given by:

$$F(s) = \frac{\sum_{m=0}^{M} \alpha_m s^m}{\sum_{p=0}^{P} \beta_p s^p}. \tag{9}$$

considering that $M \leq P$.

The PD output is given by:

$$v_d(t) = k_m v_i(t) v_o(t), \tag{10}$$

where k_m is the PD gain.

The VCO frequency is controlled according to:

$$\dot{\varphi}_o(t) = k_o v_c(t), \tag{11}$$

where k_o is the VCO gain, and v_c is the filter output given by the convolution:

$$v_c(t) = f(t) * v_d(t). \tag{12}$$

The loop gain G is defined as folows:

$$G = \frac{1}{2} k_m k_o \mathrm{v}_o A_c. \tag{13}$$

Considering the foregoing relations, the convolution theorem [13] and the trigonometric identity $\sin(A)\cos(B) = \frac{1}{2}\left[\sin(A-B) + \sin(A+B)\right]$, the dynamics of the phase error is given by:

$$L\left[\vartheta\right] + GQ\left[\Lambda(t)\big(\sin(\vartheta(t)) + \sin(2(\omega_c t + \varphi_c(t)) - \vartheta(t))\big)\right] = L\left[\varphi_o(t)\right] \tag{14}$$

The trigonometric identity is applied into equation 10 in order to transform the product of trigonometric functions into a sum. The term with $\sin(A-B)$ yields the phase difference term, and the term with $\sin(A+B)$ yields the double frequency term.

where $\Lambda(t) = \frac{A(t)}{A_c}$. The operators Q and L depend on the filter transfer function (Eq. 9), and are given by:

$$Q[\cdot] = \sum_{m=0}^{M} \alpha_m \frac{d^m}{dt^m}(\cdot), \tag{15}$$

$$L[\cdot] = \sum_{p=0}^{P} \beta_p \frac{d^{p+1}}{dt^{p+1}}(\cdot). \tag{16}$$

Second-order Sallen-Key filter

The filter considered is a second-order Sallen-Key filter shown in Fig. 5, with transfer function given by:

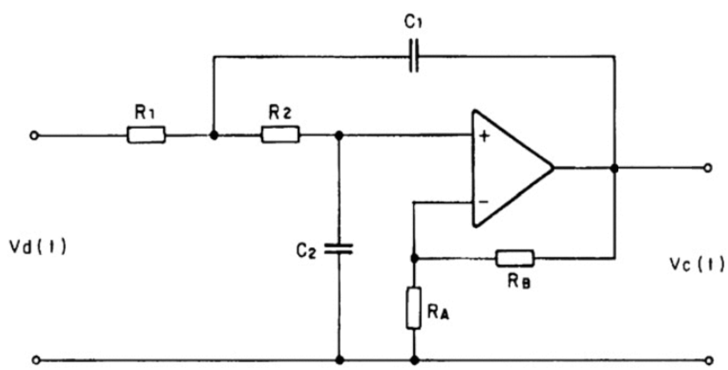

Fig. 5. Sallen and Key filter

$$F(s) = \frac{\mu\omega_n^2}{s^2 + \frac{\omega_n}{Q}s + \omega_n^2} \tag{17}$$

with

$$\omega_n^2 = \frac{1}{R_1 R_2 C_1 C_2}, \tag{18}$$

$$Q = \frac{1}{\omega_n \left[C_2(R_1 + R_2) + R_1 C_1 (1-\mu)\right]}, \tag{19}$$

and

$$\mu = 1 + \frac{R_A}{R_B}. \tag{20}$$

For $R_1 = R_2 = R$ and $C_1 = C_2 = C$ in equations 17 to 20, the transfer function of the "equal component" Sallen-Key filter [14] becomes:

$$F(s) = \frac{\mu\omega_n^2}{s^2 + (3-\mu)\omega_n s + \omega_n^2}. \tag{21}$$

2.4 The complete FM-AFM control system model

Considering what was shown above the complete model of the FM-AFM is given by the following set of equations:

$$\ddot{z}(t) + \gamma\dot{z}(t) + \omega_c^2 z(t) = r(t)\mathrm{v}_o \sin(\omega_c t + \varphi_o(t)) + \frac{A_H}{6(d(t)+z(t))^2}, \tag{22}$$

$$\dot{A}(t) + \tau_d A(t) = \tau_d z_d(t), \tag{23}$$

$$\dddot{\vartheta} + (3-\mu)\omega_n\ddot{\vartheta} + \omega_n^2\dot{\vartheta} + \mu\omega_n^2 G\Lambda(t)\sin\vartheta = \omega_n^2\Omega \tag{24}$$

$$r(t) = \Phi_{AGC}\left(A_c - A(t)\right), \tag{25}$$

$$d(t) = \Phi_{ADC}\left(\Delta\omega_c - \dot{\varphi}_0(t)\right). \tag{26}$$

where Eqs 22, 23 and 24 are the micro-cantilever, amplitude detector and PLL mathematical models, respectively. Additionally, equations 25 and 26 are the control law for the AGC and ADC systems, respectively.

In Equation 24, the double frequency term was dropped since it is supposed to be cut by the low pass filter, however, the double frequency jitter is always present, and depending on the system requirements it must be considered [9,10,12].

3 PLL lock-in range

Equation 24 represents the dynamics of a third-order PLL on a cylindrical phase surface, *i. e.*, a complete analysis of the PLL behavior can be performed considering $\vartheta \in (-\pi, \pi]$. In this case the synchronous state corresponds to a constant phase error ϑ and null frequency and acceleration errors $\dot{\vartheta} = \ddot{\vartheta} = 0$ for $t > t_s$ [7,12,15].

The lock-in range for the Sallen-Key third-order PLL is composed of the set of the values of the loop gain G, of the filter gain μ, of the filter cutoff frequency ω_n and of the microcantilever resonant frequency shift Ω for which equation 24 presents an asymptotically stable synchronous state $\left(\vartheta, \dot{\vartheta}, \ddot{\vartheta}\right) = (\vartheta^*, 0, 0)$ with $\vartheta \in (-\pi, \pi]$. In this case it is considered that $\Lambda(t) = 1$ for all t. The lock-in range can be determined with the bifurcation analysis of equation 24, which can be transformed into state space equations by defining:

$$\begin{aligned} x_1 &= \vartheta(t) \\ x_2 &= \dot{\vartheta}(t) \\ x_3 &= \ddot{\vartheta}(t) \end{aligned} \tag{27}$$

resulting in

$$\begin{aligned} \dot{x}_1 &= x_2 \\ \dot{x}_2 &= x_3 \\ \dot{x}_3 &= \omega_n^2 \Omega - (3-\mu)\omega_n x_3 - \omega_n^2 x_2 - \mu\omega_n^2 G \sin(x_1). \end{aligned} \tag{28}$$

The Jacobian matrix is given by:

$$J\Big|_{x_1 = x_1^*} = \begin{bmatrix} 0 & 1 & 0 \\ 0 & 0 & 1 \\ -\mu\omega_n^2 G \cos(x_1^*) & -\omega_n^2 & -(3-\mu)\omega_n \end{bmatrix}, \tag{29}$$

and consequently, the characteristic polynomial by:

$$P(\lambda) = \lambda^3 + (3-\mu)\omega_n\lambda^2 + \omega_n^2\lambda + \mu\omega_n^2 G \cos(x_1^*). \tag{30}$$

For $x_1 \in (-\pi, \pi]$, $x_2 = x_3 = 0$ and from equation 28 the equilibrium points can be determined by:

$$x_1^* = \sin^{-1}\left(\frac{\Omega}{\mu G}\right). \tag{31}$$

It can be seen from equation 31 that for

$$|\Omega| > \mu G \tag{32}$$

there is no synchronous state. Additionally, for $|\Omega| = \mu G$, and from equation 30, there are two non-hyperbolic syncronous states, namely, $\left(\frac{\pi}{2}, 0, 0\right)$ and $\left(-\frac{\pi}{2}, 0, 0\right)$, for $\Omega > 0$ and $\Omega < 0$, respectively.

For $|\Omega| < \mu G$ there are four synchronous states. Two for $\Omega > 0$, given by: $\mathbf{x}^{*,1} = \left(x_1^{*,1}, 0, 0\right)$ and $\mathbf{x}^{*,2} = \left(\pi - x_1^{*,1}, 0, 0\right)$; and another two for $\Omega < 0$, given by: $\mathbf{x}^{*,3} = \left(-x_1^{*,1}, 0, 0\right)$ and $\mathbf{x}^{*,4} = \left(-\left(\pi - x_1^{*,1}\right), 0, 0\right)$.

Since $\mathbf{x}^{*,2}$ and $\mathbf{x}^{*,4}$ are respectively located on the third and fourth quadrants, it follows from the Routh-Hurwitz criterion [16] and the characteristic polinomial (equation 30) that both are unstable for any parameters combination.

On the other hand, $\mathbf{x}^{*,1}$ and $\mathbf{x}^{*,3}$ can be stable or not, depending on the parameters combination. In addition, since $\cos\left(x_1^{*,1}\right) = \sqrt{1 - \left(\frac{\Omega}{\mu G}\right)^2} = \sqrt{1 - \left(\frac{-\Omega}{\mu G}\right)^2} = \cos\left(-x_1^{*,1}\right) = \cos\left(x_1^{*,3}\right)$ the characteristic polynomial can be rewritten as:

$$P(\lambda) = \lambda^3 + (3-\mu)\omega_n\lambda^2 + \omega_n^2\lambda + \mu\omega_n^2 G\sqrt{1-\left(\frac{\Omega}{\mu G}\right)^2}, \tag{33}$$

and, consequently, the stability analysis performed on the characteristic polinomial of equation 33 is valid for both $\mathbf{x}^{*,1}$ and $\mathbf{x}^{*,3}$, i.e., for $\Omega > 0$ and $\Omega < 0$, respectively.

The stability of $\mathbf{x}^{*,1}$ and $\mathbf{x}^{*,3}$ can be determined by the Routh-Hurwitz criterion. Therefore, the Routh-Hurvitz matrix is written as follows:

$$R = \begin{bmatrix} 1 & \omega_n^2 \\ (3-\mu)\,\omega_n & \mu\omega_n^2 G\sqrt{1-\left(\frac{\Omega}{\mu G}\right)^2} \\ \frac{(3-\mu)\omega_n^2 - \mu\omega_n G\sqrt{1-\left(\frac{\Omega}{\mu G}\right)^2}}{3-\mu} & 0 \\ \mu\omega_n^2 G\sqrt{1-\left(\frac{\Omega}{\mu G}\right)^2} & 0 \end{bmatrix}.$$

The synchronous states $\mathbf{x}^{*,1}$ and $\mathbf{x}^{*,3}$ are asymptoticaly stable if all elements in the first column of R are positive. Consequently, μ that is greater than 1, due to the construction of the filter, must be lower than 3, or concisely:

$$1 < \mu < 3. \tag{34}$$

In addition, $(3-\mu)\,\omega_n^2 - \mu\omega_n G\sqrt{1-\left(\frac{\Omega}{\mu G}\right)^2}$ must be positive, and for physical meaningful parameters, it results that:

$$G < \frac{1}{\mu}\sqrt{(3-\mu)^2\omega_n^2 + \Omega^2}. \tag{35}$$

Inequality 34 defines the lower and upper bounds for the lock-in range of the filter gain μ, and inequality 35 defines the upper bound of the loop-gain G. The Lower bound of G is defined by the synchronous states existence condition (equation 32), resulting that:

$$G \geq \frac{|\Omega|}{\mu}. \tag{36}$$

The inequalities 34, 35 and 36 define the lock-in range for the Sallen-Key third-order PLL. For design purposes the lock-in range must be defined for $\Omega = \Omega_{max}$, i. e., the maximun microcantilever resonant frequency shift possible for a given scanning of a sample. As an exemple, Figs. 6 and 7 show the lower bound of the lock-in range and the lock-in range for $\Omega = \Omega_{max} = 200\pi rad/s$ (100Hz).

The existence of the synchronous states is determined by a saddle-node bifurcation, represented by the lower bound of the lock-in range. For parameter values lower than the critical value, there are no equilibrium solutions, i.e., a constant phase error ϑ and null frequency and acceleration errors $\dot{\vartheta} = \ddot{\vartheta} = 0$ for $t > t_s$ [7,12,15]. On the other hand, for parameter values higher than the

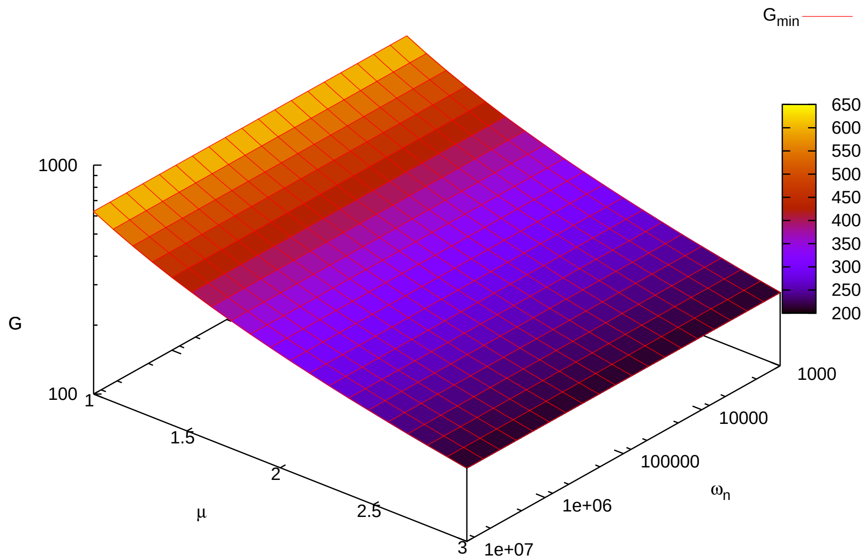

Fig. 6. Lower bound of the lock-in range for the third order Sallen-Key PLL

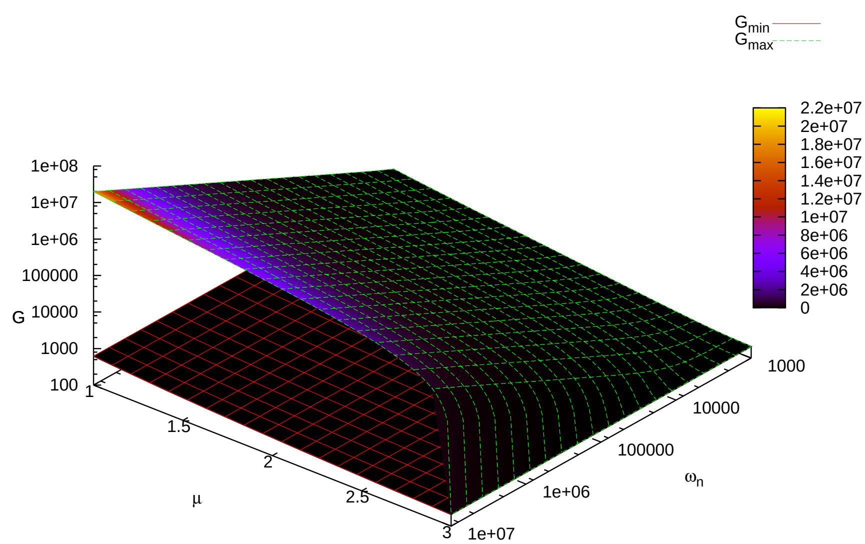

Fig. 7. Lock-in range for the third order Sallen-Key PLL

critical values, there are four hyperbolic equilibrium solutions, two stable, and two unstable.

The upper bound of the lock-in range is given by a Hopf bifurcation, generating a family of periodic solutions (limit-cycles) for loop gains above the upper bound [7,17]. Therefore, combining the lower bound, given by the saddle-node bifurcation, with the upper bound, given by the Hopf bifurcation, it can be concluded that the lock-in range for the third order PLL with second-order Sallen-Key filter is represented by the region between the two surfaces as shown in Fig. 7.

4 Simulations results

In this section some simualtion results are presented in order to illustrate the PLL behavior concerning the lock-in range and the frequency demodulation process. The simulations are performed built-in Simulink blocks, using the 4^{th} order Runge-Kutta integration algorithm. The central frequency ω_c is $200\pi \times 10^3 rad/s$ (100kHz).

The loop filter used in the simulation is a Butterworth Sallen-Key filter [14] with parameters set to $\omega_n = \frac{\omega_c}{100}$ and $\mu = 1.5858$. In accordance with inequality 35 and for $\Omega = \Omega_{max} = 200\pi rad/s$ it results that $G_{max} < 5.6174 \times 10^3$, and from inequality 36 $G_{min} > 396.2189$. The simulations results are shown in Figs. 8, 9 and 10.

The simulations results in Fig. 8 show the response of the PLL operating inside the lock-in range. Figs. 8(a), 8(c) and 8(e) show the phase error response for $G = G_{min}$, $G = 0.4G_{max}$ and $G = 0.8G_{max}$, respectively. Since the PLL designed is a type 1 system it presents steady state phase error and, as expected, the bigger the loop gain G the lower the stead state error.

Likewise, Figs. 8(b), 8(d) and 8(f) show the frequency demodulation response of the PLL to the FSK signal with amplitude Ω_{max}, for $G = G_{min}$, $G = 0.4G_{max}$ and $G = 0.8G_{max}$, respectively. It can be noticed that the bigger the loop gain G the more oscillatory the frequency demodulation response. On the other hand, the settling time is bigger for loop gains set near the boundaries of the lock-in range.

Fig. 9 show simulations responses to loop gains above the upper bound of the lock-in range. Since the upper bound represents a Hopf bifurcation Figs. 9(a) and 9(b) show the onset of a limit-cycle [17]. Additionaly, the limit-cycle amplitude increases over the loop gain G.

In addition, Fig. 10 show the simulations responses for loop gains G set bellow the lower bound of the lock-in range. The lower bound represents the saddle-node bifurcation and, as mentioned earlier, it indicates that bellow this boundary there are no syncronous states. Accordingly, in Fig. 10(a) it can be seen that the phase error increases over time, also, in Fig. 10(b) it is clear that the FSK signal Ω_{max} is not properly demodulated.

5 Conclusion

The PLL performance is vital to the FM-AFM and, accordingly, it must be properly designed in order to assure the correct demodulation of the tip and

The type of de system is given by the number of the poles of the PLL open loop transfer function located at the origin ($s = 0$) [16].
Frequency Shift Keying

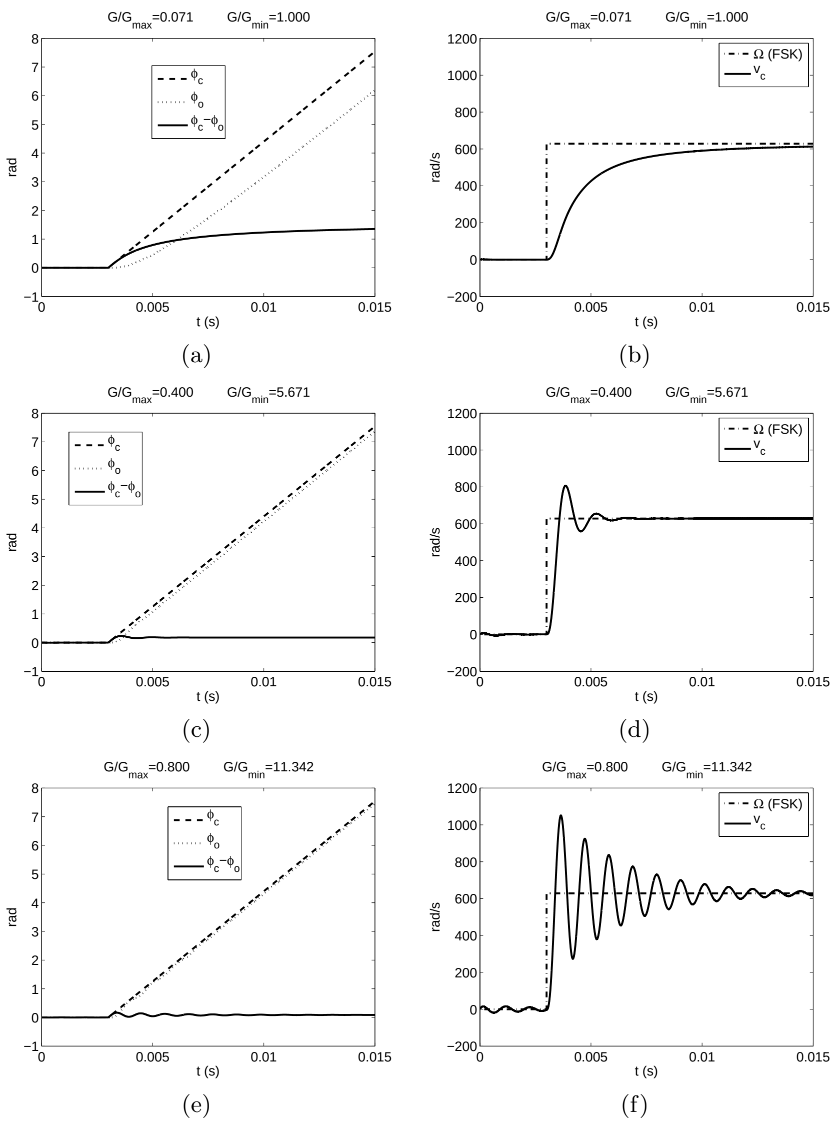

Fig. 8. Simulations with $G_{min} \leq G < G_{max}$.

sample interactions from the microcantilever motion. Here, the lock-in range for a third-order PLL with second-order Sallen-Key filter is determined, and simulations supporting the theoretical results are shown, giving hints on how to determine the PLL parameters in order to assure the existence of synchronous states, and how to improve the PLL performance.

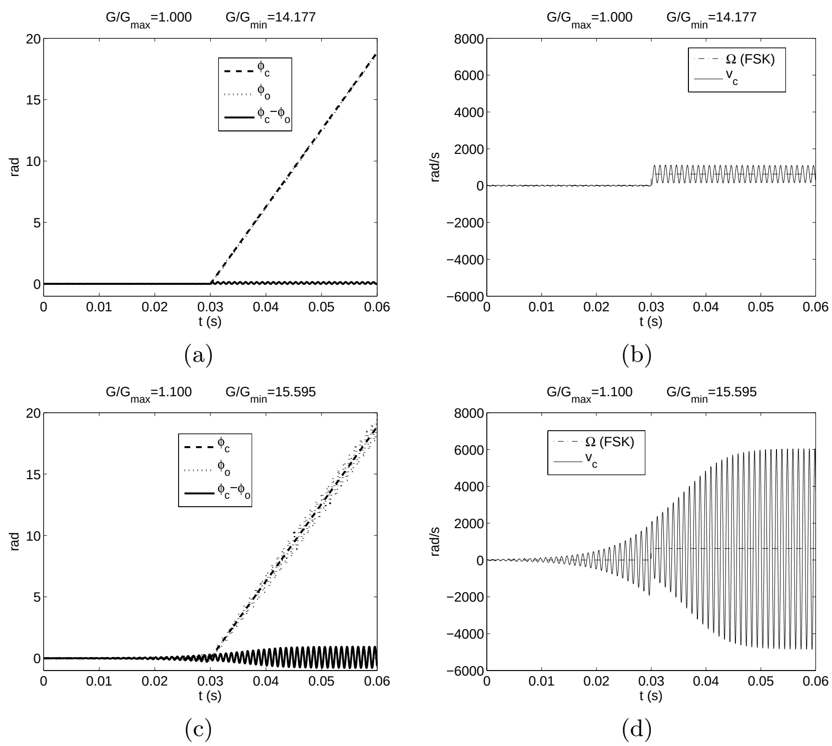

Fig. 9. Simulations with $G \geq G_{max}$.

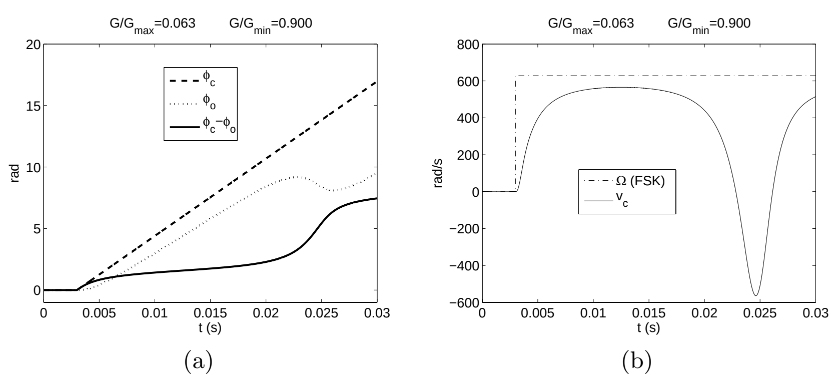

Fig. 10. Simulations with $G < G_{min}$.

References

1.G. Binnig, C. Quate, and C. Gerber. Atomic force microscope. *Physical Review Letters*, 56(9):930–933, Mar. 1986.

2.S. Morita, R. Wiesendanger, E. Meyer, and F. J. Giessibl. *Noncontact atomic force microscopy*. Springer, Berlin, 2009.

3.B. Bhushan. *Springer handbook of nanotechnology*. Springer, Berlin, 2004.

4.A. M. Bueno, J. M. Balthazar, and J. R. C. Piqueira. Phase-locked loop design applied to frequency-modulated atomic force microscope. *Communications in Nonlinear Science and Numerical Simulation*, In Press, Corrected Proof:–, 2011.
5.G. Couturier, J. Aimé, J. Salardenne, and R. Boisgard. A virtual non contact-atomic force microscope (nc-afm): Simulation and comparison with analytical models. *Eur. Phys. J. AP*, 15(2):141–147, aug 2001.
6.J. Polesel-Maris and S. Gauthier. A virtual dynamic atomic force microscope for image calculations. *Journal of Applied Physics*, 97(4):044902, 2005.
7.J. R. C. Piqueira. Using bifurcations in the determination of lock-in ranges for third-order phase-locked loops. *Communications in Nonlinear Science and Numerical Simulation*, 14(5):2328–2335, 2009.
8.A. M. Bueno, A. G. Rigon, A. A. Ferreira, and J. R. C. Piqueira. Design constraints for third-order pll nodes in master-slave clock distribution networks. *Communications in Nonlinear Science and Numerical Simulation*, 15(9):2565 – 2574, 2010.
9.F. M. Gardner. *Phaselock Techniques*. John Wiley & Sons, Inc., 3 edition, 2005.
10.R. E. Best. *Phase-Locked Loops - Design, Simulation, and Applications*. McGraw Hill Education. McGraw Hill Education, 5 edition, 2003.
11.A. M. Bueno, A. A. Ferreira, and J. R. C. Piqueira. Fully connected pll networks: How filter determines the number of nodes. *Mathematical Problems In Engineering*, 2009(Article ID 256765):13 pages, 2009.
12.A. M. Bueno, A. A. Ferreira, and J. R. C. Piqueira. Modeling and filtering double-frequency jitter in one-way master slave chain networks. *Circuits and Systems I: Regular Papers, IEEE Transactions on*, 57(12):3104 –3111, 2010.
13.T. Kailath. *Linear Systems*. Prentice-Hall information and system science series. Englewood Cliffs, N.J. : Prentice-Hall, 1980.
14.H. M. Berlin. *Design of Active Filter With Experiments*, volume 1 of *Blacksburg Continuing Education Series*. Howard W. Sams & Co., Inc., 1 edition, 1977.
15.J. R. C. Piqueira and L. H. A. Monteiro. All-pole phase-locked loops: calculating lock-in range by using evan's root-locus. *International Journal of Control*, 79(07):822–829, July 2006.
16.K. Ogata. *Modern Control Engineering*. Prentice Hall, 2002.
17.J. Guckenheimer and P. Holmes. *Nonlinear Oscillations, Dynamical Systems, and Bifurcations of Vector Fields*, volume 42 of *Applied Mathematical Sciences*. Springer, 2 edition, 1983.